A Theoretical Analysis of the Weak-beam Method of Electron Microscopy

D. J. H. COCKAYNE

Department of Metallurgy, University of Oxford

(Z. Naturforsch. 27 a, 452—460 [1972]; received 27 December 1971)

Dedicated to Prof. Dr. K. MOLIÈRE *on his 60-th birthday*

The geometry of lattice defects can be studied in detail using the weak-beam method [1] of high resolution electron microscopy. In this paper the theoretical basis of the method is discussed, and the experimental conditions which are necessary if particular methods of image interpretation are to be used are considered.

§ 1. Introduction

In electron microscope studies of lattice defects, two of the principle features of interest are the geometry and character of the individual defects, or defect elements. Many of these defect systems require image analysis at high resolution (e.g. the dissociation of dislocations in pure metals; the study of small point defect clusters) and the weak-beam method of electron microscopy [1] enables systematic analyses to be carried out at a resolution approaching the resolution capabilities of the electron microscope. In this paper, the theoretical basis for the method is discussed, and some approximate methods for interpreting the images are deduced. The experimental conditions which are necessary to obtain weak-beam images, and to use these methods of interpretation, are considered.

Other than studies using the weak-beam method, high resolution electron microscope investigations of defect structures have followed two courses. One of these is to form lattice fringe images from crystals containing defects and to deduce the defect structure from the perturbations of the fringes. However, it has been shown recently [2] that the interpretation of such images is more complicated than has generally been assumed. The second method is to form dark- or bright-field images with the lattice oriented near to the Bragg condition for the dark-field reflection in order to optimise the image contrast while keeping the image intensity appreciable (so-called "strong-beam" conditions). Where such images do not enable the defect structure to be determined unambiguously, or in sufficient detail, or where some doubt arises as to the character of the defect, the strong-beam images can be compared with computer simulated images [3] calculated for the various postulated defect models. To a large extent, these computer simulation studies depend upon image properties which are related to the geometry of the defect system through dynamical scattering effects (e.g. the depth dependence of the image). However, in many high resolution studies (e.g. the investigation of the geometry of dissociated dislocations in silicon [4]) no model is known a priori, and it is desirable that the image be related in an obvious way to the dislocation geometry, so that a model for the defect system can be postulated. In particular, for systematic high resolution studies, the images should have the following properties:

(1) each dislocation core should give rise to an image peak, the position of which defines the position of the core.

(2) for high resolution studies of closely spaced cores, the half-width of the image from each core should approach the experimental recording capabilities.

(3) the invisibility criteria (i.e. $\boldsymbol{g} \cdot \boldsymbol{b} = 0$ and $\boldsymbol{g} \cdot \boldsymbol{b} \wedge \boldsymbol{u} = 0$, where $\boldsymbol{b}$ is the dislocation Burgers vector, $\boldsymbol{g}$ is the reciprocal lattice vector for the imaging reflection and $\boldsymbol{u}$ is a unit vector in the direction of the dislocation line) should apply to the image peak from each core in a system separately, so that the character and geometry of the individual elements can be determined.

(4) the image should be insensitive to small changes in lattice orientation, foil thickness and dislocation depth. If this condition is obtained, an accurate knowledge of these parameters, which are difficult to determine experimentally, is not necessary. However it may be preferable in partic-

Reprint requests to Dr. D. J. H. Cockayne, University of Oxford, Department of Metallurgy, Parks Road, *Oxford*, England.

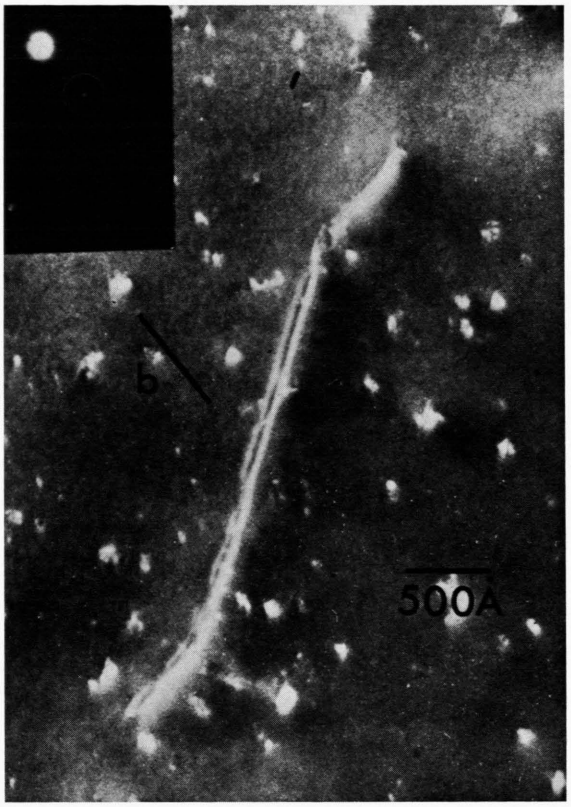

Fig. 1. The weak-beam image peaks are seen for a dissociated dislocation in silver[6] taken with $\boldsymbol{g} \cdot \boldsymbol{b} = 2$. The diffraction pattern is inset, with the weak-beam circled.

ular instances to relax this condition in order to utilise the information contained in the depth dependence of the image (as in the determination of the character of point defect clusters in strong-beam images).

Provided that certain experimental conditions (discussed in §§ 5 and 6) are satisfied weak-beam images have all the properties outlined above. An example is shown in Fig. 1* for a dissociated dislocation in silver, and the image peak from each partial is clearly observed. Such images have been used, for example, to determine the equilibrium spacing of partial dislocations in pure f.c.c. metals (see [5,6]) and to investigate the geometry of dissociated dislocations in silicon[4].

The discussion in this paper is restricted to those situations in which the column approximation applies[7], a restriction which may become important when defect detail below 25 Å is to be investigated[8]. It is emphasised that the dislocation systems considered are idealised (i.e. isotropic elasticity, no surface effects) to enable the principles of the weak-beam method to be more easily appreciated. The many-beam computed images discussed are for 100 keV electrons, with six systematic reflections and absorption[9] taken into account.

§ 2. The Weak-beam Method

The weak-beam method derives from computed many-beam images which show that dark-field images of dislocations, for those reflections whose reciprocal lattice points are far from the Ewald sphere, have narrow peaks with intensity many times background and lying close to the projection of the dislocation core. An example is shown in Fig. 2 for a dissociated edge dislocation in copper lying parallel to the foil surface. The most noticeable features of these images are the narrowness of the image peaks and the invariance of the peak positions for different foil thicknesses. Similar features are observed for dislocations lying at different foil depths. It was observed that the positions of the image peaks are in close agreement with the following physical concept: if a lattice containing a defect is oriented sufficiently far from the Bragg condition for a reciprocal lattice point $\boldsymbol{g}$ (where the term "sufficiently far" is discussed in § 5) then the image taken with the diffracted beam $\boldsymbol{g}$ shows an intensity peak for those parts of the lattice which are brought into the Bragg condition by the defect strain field. This means that if $\boldsymbol{R}(z)$, the lattice displacement at depth z in the lattice, is a continuously varying function of z, then the image peak occurs for those columns in the lattice in which $s_g + \boldsymbol{g} \cdot \mathrm{d}\boldsymbol{R}(z)/\mathrm{d}z = 0$ at a turning point of $\boldsymbol{g} \cdot \mathrm{d}\boldsymbol{R}(z)/\mathrm{d}z$ (where s_g is the distance of the reciprocal lattice point $\boldsymbol{g}$ from the Ewald sphere, measured in the z direction).

In Fig. 2, the positions of the image peak predicted by this criterion are marked W, and are seen to be close to the positions of the image peaks computed using six-beam dynamical theory.

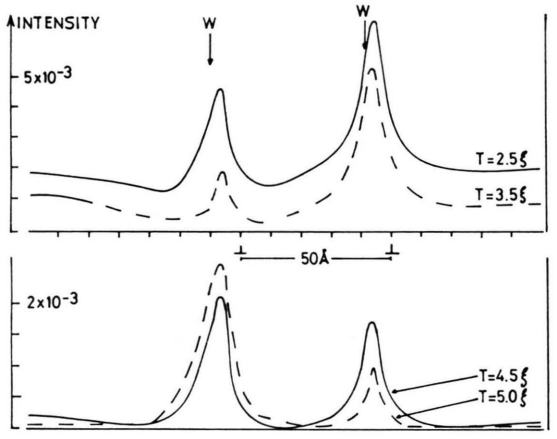

Fig. 2. Computed weak-beam images of a dissociated edge dislocation in copper lying at depth ξ_{220} in (111) foils of various thicknesses (as indicated). W are the peak positions predicted using the criterion discussed in § 2. The images are for $g = 2\bar{2}0$,

$$\boldsymbol{b} = \frac{a}{2}[1\bar{1}0] \rightarrow \frac{a}{6}[1\bar{2}1] + \frac{a}{6}[2\bar{1}\bar{1}],$$

$$\boldsymbol{u} = \frac{1}{\sqrt{6}}[11\bar{2}], \quad |s_g| = 2 \times 10^{-2}\,\text{Å}^{-1}.$$

and unit incident beam intensity.

Numerous computed images[10] of dissociated and undissociated dislocations in copper and silicon, in orientations from screw to edge, and at various depths in foils from thickness ξ_g to $6\xi_g$ (where ξ_g is the extinction distance defined in § 3) verify that the peak positions of images taken in $g = \langle 220 \rangle$ do not deviate by more than 7 Å from the position W given by the above criterion provided that $|s_g| > 2 \times 10^{-2}\,\text{Å}^{-1}$ (and with a further condition discussed in § 5). This makes clear the

* Fig. 1 see p. 452 a.

value of the criterion in determining the position of the dislocation core from the image peak position.

The ability to interpret the position of the image peak by a physical argument such as that given above is not essential to the usefulness of weak-beam images, and for studies at very high resolution it may be necessary to derive the relationship between the image peak position and the strain field by more careful analyses such as those discussed in § 3, or alternatively by computer simulated images.

§ 3. Bloch Wave Analysis of Weak-beam Images

In order to place the condition for obtaining weak-beam images on a quantitative basis, we consider the many-beam dynamical theory for scattering by an imperfect lattice. The theories generally used imply the so-called column approximation[7], where along a given line of propagation of the electron beam (usually chosen as the z axis normal to the crystal surface) the crystal is imagined to behave as a superposition of elementary crystal slabs, each perfect but displaced by amounts $\boldsymbol{R}(z)$, z denoting the depth of the slab from the top surface of the crystal. In this approximation, the wave function can be expressed as

$$\Psi(\boldsymbol{r}) = \sum_g \varphi_g(z) \exp\{2\pi i(\boldsymbol{\chi} + \boldsymbol{g})\,\boldsymbol{r}\} \qquad (1)$$

where $\boldsymbol{\chi}$ is the vacuum wave vector. Alternatively, in the Bloch wave formulation

$$\Psi(\boldsymbol{r}) = \sum_j \psi^{(j)}(z) \sum_g C_g{}^{(j)} \exp\{2\pi i(\boldsymbol{k}^{(j)} + \boldsymbol{g})\,\boldsymbol{r}\} \qquad (2)$$

where $\psi^{(j)}(z)$ is the amplitude of the jth Bloch wave and $C_g{}^{(j)}$ is the gth element of the jth eigenvector of the matrix

$$A = \begin{pmatrix} 0 & \frac{1}{2\xi_g} & \frac{1}{2\xi_h} & \cdot \\ \frac{1}{2\xi_g} & s_g & \frac{1}{2\xi_{g-h}} & \cdot \\ \frac{1}{2\xi_h} & \frac{1}{2\xi_{g-h}} & s_h & \cdot \\ \cdot & \cdot & \cdot & \cdot \end{pmatrix}. \qquad (3)$$

and $\gamma^{(j)} = k_z{}^{(j)} - K_z$ is the jth eigenvalue. K_z and $k_z{}^{(j)}$ are the z components of the incident wave vector after refraction by the mean inner potential of the crystal and of $\boldsymbol{k}^{(j)}$ respectively;

$$\xi_g = (2m\,e/h^2)\,V_g$$

where V_g is the Fourier coefficient of the crystal potential. For simplicity a centrosymmetric crystal potential has been assumed (for further details see Hirsch, Howie, Nicholson, Pashley and Whelan[11]). From Eqs. (1) and (2)

$$\varphi_g(z) = \sum_j \psi^{(j)}(z)\, C_g{}^{(j)} \exp(2\pi i\, \gamma^{(j)} z). \qquad (4)$$

The wave function for an imperfect crystal, within the column approximation, can be expressed as[11]

$$\Psi(\boldsymbol{r}) = \sum_j \psi^{(j)}(z) \sum_g C_g{}^{(j)} \cdot \exp\{2\pi i(\boldsymbol{k}^{(j)} + \boldsymbol{g})\,\boldsymbol{r}\} \exp\{-2\pi i\,\boldsymbol{g}\cdot\boldsymbol{R}\}.$$

When this expression for $\Psi(\boldsymbol{r})$ is substituted in the Schrödinger wave equation, and the second derivatives are neglected[12], the differential equations for scattering of Bloch waves are obtained:

$$\frac{\mathrm{d}\psi^{(j)}(z)}{\mathrm{d}z} = \sum_l \psi^{(l)}(z) \sum_g \left\{ 2\pi i \frac{\mathrm{d}\boldsymbol{g}\cdot\boldsymbol{R}}{\mathrm{d}z} C_g{}^{(j)*} C_g{}^{(l)} \right\} \cdot \exp\{2\pi i(k_z{}^{(l)} - k_z{}^{(j)})\,z\} \qquad (5)$$

where $k_z{}^{(l)}$ is the z component of $\boldsymbol{k}^{(l)}$.

We introduce the notation

$$R^{jl}(z) = 2\pi i\,\boldsymbol{g}\cdot\boldsymbol{R}\, C_g{}^{(j)*} C_g{}^{l}$$

and

$$\Delta k^{jl} = k_z{}^{(l)} - k_z{}^{(j)}.$$

Then by expanding

$$\frac{d}{\mathrm{d}z}\left[\psi^{j}(z) \exp\left(-\sum_g R^{jj}(z)\right)\right]$$

and using Eq. 5 the following expression for $\psi^{(j)}(t)$ is obtained:

$$\psi^{(j)}(t) = \exp\left\{\sum_g R^{jj}(t)\right\} \cdot \left\{ \int_0^t \sum_{l\neq j} \psi^{(l)}(z) \sum_g \frac{\mathrm{d}R^{jl}(z)}{\mathrm{d}z} \exp\{2\pi i\,\Delta k^{jl} z\} \cdot \exp\left\{-\sum_g R^{jj}(z)\right\} \mathrm{d}z + \psi^{(j)}(0) \right\}. \qquad (6)$$

The analysis to this point, and taking $\psi^{l}(z)$ as constant, is equivalent to the treatment of Wilkens[13].

This equation expresses the amplitude of the jth Bloch wave at depth t as the amplitude of the jth Bloch wave at the entrance face of the crystal together with contributions from all other Bloch waves ($l \neq j$) arising through scattering by the strain field $\mathrm{d}R^{jl}(z)/\mathrm{d}z$. We now make the assumption (discussed in § 4) that, in the integral of Eq. (6),

each $\psi^l(z)$ can be assumed to be constant. Considering the integral in three parts, $\alpha_i < z < \alpha_{i+1}$ where $\alpha_1 = 0$, $\alpha_2 = \alpha$, $\alpha_3 = \beta$ and $\alpha_4 = t$ as in Fig. 3, and integrating Eq. 6 by parts, we obtain

$$\psi^{(j)}(t) = \exp\Big(\sum_g R^{jj}(t)\Big) \cdot \Big(\sum_{l \neq j} B^{lj}\, \psi^{(l)} < \sum_{i=1,3} F_i > + \psi^{(j)}(0)\Big) \tag{7}$$

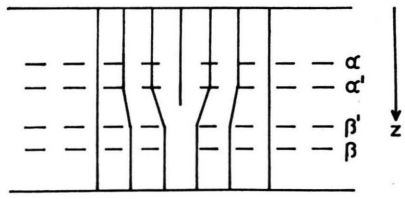

Fig. 3.

where

$$F_i = 2\pi i\, \Delta k^{lj} \int_{\alpha_i}^{\alpha_{i+1}} \exp\{2\pi i (\Delta k^{lj} z - \sum_g \boldsymbol{g}\cdot\boldsymbol{R}\, C_g^{(j)*} C_g^{(j)})\}\, dz - [\exp\{2\pi i (\Delta k^{lj} z - \sum_g \boldsymbol{g}\cdot\boldsymbol{R}\, C_g^{(j)*} C_g^{(j)})\}]_{\alpha_i}^{\alpha_{i+1}}$$

and

$$B^{lj} = \sum_n n\, C_n^{(j)*} C_n^{(l)} / \sum_n n\, C_n^{(j)*} C_n^{(j)}.$$

We now define $R(0) = 0$, and assume that $R(z) = R(0)$ for $z < \alpha'$ and $R(z) = R(t)$ for $z > \beta'$. Then it is possible to choose $\alpha < \alpha'$ and $\beta > \beta'$ (see Fig. 3) such that $\Delta k^{lj}\alpha =$ integer and

$$\Delta k^{lj}\beta - \sum_g \boldsymbol{g}\cdot\boldsymbol{R}\, C_g^{(j)*} C_g^{(j)} = \text{integer}.$$

With these limits, $F_1 = F_3 = 0$ and

$$\psi^{(j)}(t) = \exp\Big(\sum_g R^{jj}(t)\Big) \cdot \Big\{\sum_{l\neq j} B^{lj}\, \psi^{(l)}\, 2\pi i\, \Delta k^{lj} \cdot \int_\alpha^\beta \exp\Big\{2\pi i \Big(\Delta k^{lj} z - \sum_g \boldsymbol{g}\cdot\boldsymbol{R}\, C_g^{(j)*} C_g^{(j)}\Big)\Big\}\, dz + \psi^{(j)}(0)\Big\}.$$

This may be written

$$\psi^{(j)}(t) = \exp\Big(\sum_g R^{jj}(t)\Big) \cdot \Big\{\sum_{l\neq j} B^{lj}\, \psi^{(l)}\, 2\pi i\, \Delta k^{lj} \cdot \int_\alpha^\beta \exp\{2\pi i\,(-S^{jl} z - \boldsymbol{g}\cdot\boldsymbol{R}^+(z))\}\, dz + \psi^{(j)}(0)\Big\} \tag{8}$$

where

$$S^{jl} = \Delta k^{jl} = k_z^{(l)} - k_z^{(j)}$$

and

$$\boldsymbol{R}^+(z) = \boldsymbol{R}(z) \sum_n n\, C_n^{(j)*} C_n^{(j)}.$$

In deriving this result from Eq. (6) we have made one assumption, which is that each $\psi^{(l)}$ remains constant over the range of the integral. With this approximation we see from Eq. (8) that the scattering into $\psi^{(j)}$ from $\psi^{(l)}$ is independent of the contributions from other Bloch waves. Further, since $\boldsymbol{R}(z)$ appears in Eq. (8) only in the term $\boldsymbol{R}^+(z)$, and since the terms outside the integral depend only upon the diffracting conditions of the perfect lattice, the contribution to $\psi^{(j)}$ from $\psi^{(l)}$ for a given crystal orientation is maximum for those conditions of the displacement field $\boldsymbol{R}^+(z)$ which maximise the integral. The relevance of this result to the weak-beam method is discussed in the next section.

§ 4. Weak-beam Images and Interband Scattering

The weak-beam condition for the reflection g requires that in the perfect lattice $|\varphi_g(z)| \ll 1$ for all z. Since in the absence of strain, $\psi^{(j)}(z) = C_0^{(j)}$, Eq. 4 implies that $|C_0^{(j)} C_g^{(j)}| \ll 1$ for all j.

In the two-beam case

$$\psi^{(1)}(0) = C_0^{(1)} = C_g^{(g)} = \cos\beta/2$$

and

$$\psi^{(g)}(0) = C_0^{(g)} = -C_g^{(1)} = \sin\beta/2$$

with $\cot\beta = w = s\xi_g$ (for the numbering of the branches of the dispersion surface, see § 5.1). For $|s| \to \infty$, $\beta = \varepsilon \cong 0$, $\psi^{(1)}(0) \cong 1$ and $\psi^{(g)}(0) \cong \varepsilon$. From Eq. (3) a change $\Delta\psi^{(j)}$ in $\psi^{(j)}$ produces a change in φ_g given by

$$|\Delta\varphi_g| = |\sum_j \Delta\psi^j\, C_g^{(j)} \exp(2\pi i\, \gamma^{(j)} z)| \cong |\Delta\psi^{(g)}(0)|$$

since $|C_g^{(g)}| \gg |C_g^{(1)}|$ and $|\psi^{(1)}(0)| \gg |\psi^{(g)}(0)|$. From this we deduce that appreciable weak-beam contrast for a reflection g occurs for those conditions which produce strong interband scattering from Bloch wave 1 to Bloch wave g (i.e. more generally, from the branch of the dispersion surface with largest $|\psi^{(j)}(0)|$ to the branch with largest $|C_g^j|$). Consequently, for $|s|$ large, the weak-beam intensity will be maximum for those conditions of Eq. 6 which produce maximum scattering from $\psi^{(1)}$ to $\psi^{(g)}$. But since $\psi^{(1)} \cong$ constant, this occurs

for those conditions of $\boldsymbol{R}^+(z)$ in Eq. (8) which maximise the integral

$$\int_{\alpha}^{\beta} \exp(-2\pi i(S^{lj} z + \boldsymbol{g}\cdot\boldsymbol{R}^+(z))\,\mathrm{d}z .$$

Approximate criteria for the weak-beam peak position can be deduced from this result as follows:

(1) In the two-beam case, $S^{lj} \to s_g$ and $\boldsymbol{R}^+(z) \to \boldsymbol{R}(z)$ as $|s_g| \to \infty$. The integral then reduces to

$$\int_{\alpha}^{\beta} \exp\{-2\pi i(s z + \boldsymbol{g}\cdot\boldsymbol{R})\}\,\mathrm{d}z$$

which is the Bloch wave form of the kinematic integral[7]. Consequently we see that in the two-beam approximation, and in the limit $|s_g| \to \infty$, weak-beam images are given by the kinematical theory. It is reasonable to assume that, for the conditions under which weak-beam images are formed, and with no strong diffracted beams present (see § 5.2), the image half-width and peak position given by the kinematical theory will be a good approximation to the many-beam computed images. This has been confirmed by DE RIDDER and AMELINCKX[14].

(2) If there is no restriction on the form of $\boldsymbol{R}(z)$, the integral is maximum when $S^{lj} z + \boldsymbol{g}\cdot\boldsymbol{R}^+(z) =$ constant ($\alpha < z < \beta$), which on differentiating gives $S^{lj} + \boldsymbol{g}(\mathrm{d}\boldsymbol{R}^+(z)/\mathrm{d}z) = 0$ ($\alpha < z < \beta$). This condition requires that the strain field is of the form shown in Figure 3. For a general strain field, in the two-beam case with $|s_g| \to \infty$, this condition approximates to satisfying the condition

$$s_g + \boldsymbol{g}(\mathrm{d}\boldsymbol{R}(z)/\mathrm{d}z) = 0$$

at a turning point of $\boldsymbol{g}(\mathrm{d}\boldsymbol{R}(z)/\mathrm{d}z)$. The fact that this result is in good accord with many-beam computed images (e.g. Fig. 2) justifies the approximation, but its accuracy will depend upon $|s_g|$ and the nature of the strain field.

As has been reported elsewhere[1,10], the many-beam computed images have image peak positions which vary between the position predicted by the kinematical theory and the position predicted by the criterion given in (2) above. This is because, as shown, both criteria are approximations to the integral of Eq. (8). Therefore if, when interpreting images using either of these two criteria, the difference between their predicted peak positions is important, then a more detailed investigation of Eq. (8), or analysis of computed images, is necessary.

§ 5. Conditions to be Satisfied for Obtaining Weak-beam Images

§ 5.1. *Conditions from two-beam theory*

When $|\beta|$ (see § 4) is small, C, the matrix of eigenvectors of A [Eq. (3)] arranged in the appropriate order, is close to diagonal. (For clarity it is necessary to explain the order of the eigenvectors chosen. Each eigenvector is associated with one branch of the dispersion surface. For a particular direction of beam incidence, the branch which is closest to the circle of radius $K = 1/\lambda$ centred on the reciprocal lattice point j is denoted as branch j. This is illustrated in Figure 4. Exceptionally,

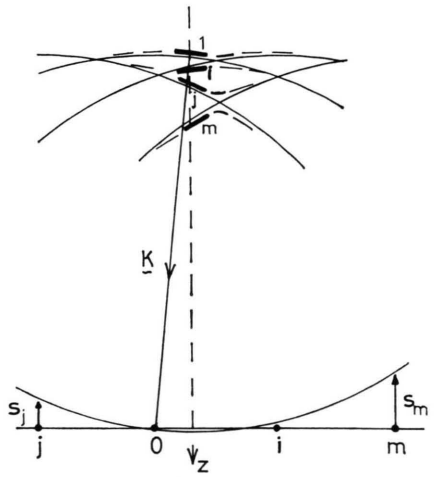

Fig. 4. The branch j of the disperion surface is that branch closest to the circle of radius $K = 1/\lambda$ centred on the reciprocal lattice point j.

branch 1 is centred on the origin. This choice of numbering of branches is different from that normally chosen, but the ordering of the eigenvectors, and hence the numbering of the branches, is arbitrary. The present choice is made to ensure that C is close to diagonal when all $|s_j|$ are large and appreciably different. It is not suggested that this terminology be adopted in general.) When C is close to diagonal, first order perturbation theory[15] can be applied to determine the relationship between the off-diagonal elements of C and the elements of A. (I am indebted to Dr. A. P. Pogany for advice on this point.) Such an analysis gives

$$\varepsilon_j{}^i = |C_j{}^i| \cong \left|\frac{A_j{}^i}{A_i{}^i - A_j{}^j}\right| = \left|\frac{1}{2\xi_{i-j}(s_i - s_j)}\right| \qquad (9)$$

which for the two-beam case is

$$\varepsilon = |C_0{}^{(2)}| = |C_g{}^{(1)}| \cong 1/2\xi_g s_g .$$

This result agrees with $\varepsilon = |\sin \beta/2|$ in the approximation that $\sin(\beta/2) = \beta/2$.

From this analysis arises the fundamental condition for obtaining weak-beam images. It has been seen in the two-beam case that provided $|\psi^{(1)}| \gg |\psi^{(g)}| = \varepsilon$ and $|C_g^{(g)}| \gg |C_g^{(1)}| = \varepsilon$, the weak-beam image arises when there is strong scattering from Bloch wave 1 into Bloch wave g. The smaller is the value of ε, the more precise will be this interpretation of the image, and the larger will be the image contrast. But the image intensity decreases with ε, so that ε is limited experimentally. A reasonable compromise is $\varepsilon \leqq 0.1$, for which $|\psi^{(1)}| \geqq 10|\psi^{(2)}|$ and computed and experimental images for these conditions (i.e. $|w| = |s\xi_g| \geqq 1/2\varepsilon = 5$) show image peaks with high contrast and with the peak position close to that given by the criteria of § 4.

The condition $|w| \geqq 5$ ensures that weak-beam images will appear as intensity peaks whose position is closely predicted by the criteria of § 4, or more accurately by Eq. (8). However it is shown in § 6 that if the images are to be used to determine geometrical parameters of defects (e.g. partial separations of dissociated dislocations), there is a lower limit to $|s|$ (rather than to $|w|$) which depends upon the accuracy of analysis required and the detail to be investigated. The condition $|w| \geqq 5$ should be considered as a limiting condition for obtaining weak-beam images which give qualitative information. (An example of such an investigation, using $|w| \sim 7$, is the study of small loops in silicon taken with $|s_g| \cong 1 \times 10^{-2}$ Å^{-1} [16].)

5. 2. *Conditions from many-beam theory*

The analysis given in § 5.1 for the two-beam case can be extended to the many-beam case. If the matrix C is close to diagonal, the off-diagonal terms are given by Equation 9. For the weak-beam g, the argument of § 5.1 now applies to Bloch waves 1 and g i.e. the weak-beam image contrast derives from scattering from Bloch wave 1 to Bloch wave g provided that $|\psi^{(1)}| \gg |\psi^{(k)}|$ (for all $k \neq 1$) and $|C_g^{(g)}| \gg |C_g^{(j)}|$ for all $j \neq g$).

The first of these conditions can be considered by referring to Eq. 9 where, if C is nearly diagonal, $|\psi^{(k)}| \cong |1/2\xi_k s_k|$. Then $|\psi^{(k)}| \ll |\psi^{(1)}|$ provided that $|1/2\xi_k s_k| = \varepsilon_0{}^k \ll 1$. For high order systematic reflections this condition is easily satisfied since in general ξ_k increases with the magnitude of k. Some care must be taken in orientating the lattice so that low order reflections are not satisfied if it is necessary that only one Bloch wave should be excited.

The second condition ($|C_g^{(g)}| \gg |C_g^{(j)}|$) can be considered in a similar way. When A is nearly diagonal, Eq. (9) gives $|C_g^{(j)}| \cong |1/2\xi_{g-j}(s_g - s_j)|$. In order that $|C_g^{(j)}| \ll |C_g^{(g)}|$, it is necessary that $s_g - s_j \neq 0$ for any reciprocal lattice point j. A little consideration of Fig. 4 shows that, when $s_g - s_j = 0$ then $s_{Ng} = 0$ where $Ng = g + j$. Consequently if the Ewald sphere passes through, or close to, the reciprocal lattice point $Ng = g + j$ then $|C_g^{(j)}|$ will be comparable with $|C_g^{(g)}|$. An example is shown in Fig. 5 for the case $g = \bar{2}\bar{2}0$ in

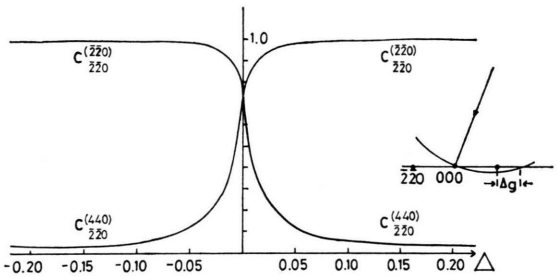

Fig. 5. The variation of $C^{(\bar{2}\bar{2}0)}_{\bar{2}\bar{2}0}$ and $C^{(440)}_{\bar{2}20}$ are shown as a function of the deviation $\Delta \cdot (\bar{2}\bar{2}0)$ from the reciprocal lattice point 220.

copper with $j = 440$. The variation of $|C_g^{(g)}|$ and $|C_g^{(j)}|$ as a function of deviation from satisfying the reflection $Ng = g + j = 220$ is shown. It is seen that provided the Ewald sphere does not cut the line of systematic reflections closer than $\Delta \cdot g = 0.06\, g$ to the reflection 220 then $|C_g^{(g)}| > 10|C_g^{(j)}|$. (A more general result can be obtained, namely $s_g - s_j = \Delta(N-2)\, g^2/2K$ where $\Delta \cdot g$ is the distance from the reciprocal lattice point $Ng = g + j$ to the point where the Ewald sphere cuts the line of systematic reflections. Consequently for $|C_g^{(j)}| = \varepsilon \leqq 0.1$,

$$|C_g^{(j)}| \cong \left|\frac{1}{2\xi_{g-j}(s_g - s_j)}\right| = \left|\frac{K}{\xi_{(N-2)g}\,\Delta\,(N-2)\,g^2}\right| \leqq 0.1.$$

This equation can be used to determine Δ in a particular case.) In general, provided that the Ewald sphere cuts the line of systematic reflections between, and not at, reciprocal lattice points, then $|C_g^{(g)}| \gg |C_g^{(j)}|$ for all $j \neq g$. These conditions can be set of course by reference to the Kikuchi pattern.

§ 5.3. *The weak-beam image when another reflection is satisfied*

Under these circumstances the discussion in § 5.2 shows that there are two terms, $|C_g^{(g)}|$ and $|C_g^{(j)}|$, which are comparably large. Then scattering from the strongly excited Bloch wave(s) to Bloch waves g and j are equally important in determining the contrast (since $\varphi_g(z) = \sum_l \psi^{(l)}(z) \cdot C_g^{(l)} \exp\{2\pi i \gamma^{(l)} z\}$). In the case when no reflection is satisfied (§ 5.2) only the term $l = g$ was important. However in the present case both $l = g$ and $l = j$ are important, provided that one of the terms is not preferentially absorbed (see § 5.4). The presence of these two terms can influence the image in three ways: (1) the weak-beam image intensity is thickness dependent, and oscillates with thickness; (2) the image peak position is thickness dependent because in Eq. (8) the conditions which give rise to the image peak involve scattering between more than two Bloch waves; (3) the image half-width broadens.

These effects are illustrated in Fig. 6 which shows computed six-beam images for a dissociated edge dislocation in copper with

$$\boldsymbol{b} = \boldsymbol{b}^1 + \boldsymbol{b}^2 = \frac{a}{6}[1\bar{2}1] + \frac{a}{6}[2\bar{1}\bar{1}]$$

lying at depth ξ_g in the plane of a (111) foil. The images, for $g = 20\bar{2}$, have $\boldsymbol{g} \cdot \boldsymbol{b}^1 = \boldsymbol{g} \cdot \boldsymbol{b}^1 \wedge \boldsymbol{u} = 0$ so that one of the partials is out of contrast (isotropic elasticity). A range of foil thicknesses has been chosen, and the images plotted for three diffracting conditions. In each case $|s_g| \cong 2 \times 10^{-2}$ Å^{-1} with the diffracting conditions being shown at the head of each column. In Figs. 6b and 6c, $|s_{\bar{g}}| \neq 0$. The image peaks have narrow (~ 15 Å) half-widths, and the peak positions are relatively thickness independent and lie close to the position predicted in § 4. On the other hand, $|s_{\bar{g}}| = 0$ for Fig. 6a and the images show perturbations of the form discussed above. The peak position is depth dependent and varies in width. Nevertheless it is clear that even these disparities will only be detectable under conditions when experimental detail ~ 15 Å can be measured.

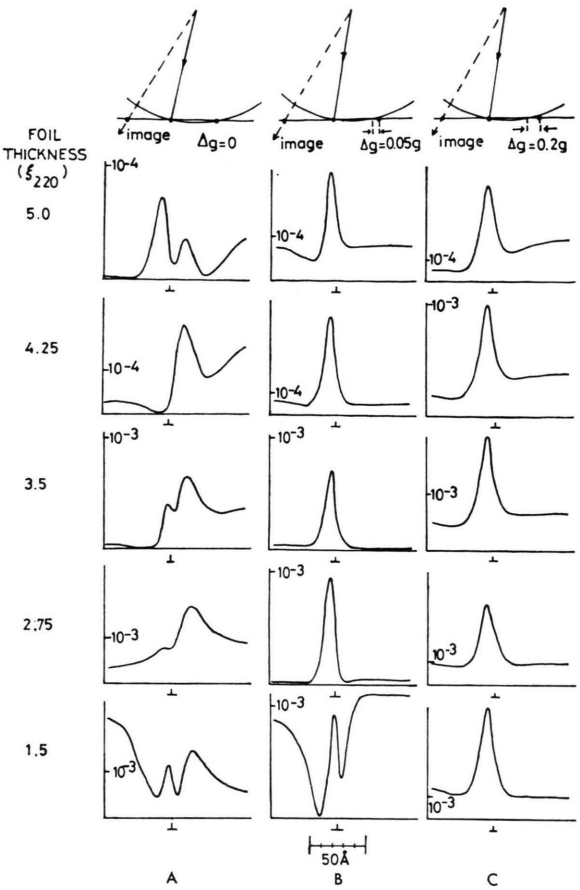

Fig. 6. Computed weak-beam images of a dissociated edge dislocation in copper lying at depth ξ_{220} in (111) foils of various thicknesses (as indicated). The images are for $g = 20\bar{2}$ and

$$\boldsymbol{b} = \boldsymbol{b}^1 + \boldsymbol{b}^2 = \frac{a}{6}[1\bar{2}1] + \frac{a}{6}[2\bar{1}\bar{1}]$$

so that $\boldsymbol{g} \cdot \boldsymbol{b}^1 = \boldsymbol{g} \cdot \boldsymbol{b}^1 \wedge \boldsymbol{u} = 0$. In each case $|s_g| \cong 2 \times 10^{-2}$ Å^{-1} but the deviation from satisfying the Bragg condition for the reciprocal lattice point $\bar{2}02$ varies, as indicated at the top of each column.

§ 5.4. *Effects of absorption*

The effects of absorption can be included by making $k^{(j)}$ complex (see e.g. HIRSCH et al.[11]). The imaginary part of $k^{(j)}$, which is responsible for absorption, depends upon both lattice orientation and j. Consequently the terms in Eq. (4) are absorbed to different extents, depending upon the lattice orientation. This effect may be of importance when optimising the conditions for obtaining high resolution weak-beam images.

§ 6. Conditions for High Resolution Studies

In the analyses of the previous sections, we have deduced the criteria which must be fulfilled for the weak-beam image for an isolated dislocation core

to appear as an intensity peak of high contrast, with the position of the image peak defining the position of the core. However this does not ensure that the peak is narrow, nor that the image peak lies close to the projection of the core, and both of these features are desirable for high resolution studies.

§ 6.1. *Conditions determined by image half-width*

It has been shown in § 4 that in the two-beam case in the limit $|s_g| \to \infty$, the weak-beam image is given by the kinematical theory. It is therefore reasonable to assume that to a first approximation, the image half-width Δx (i.e. width at half-height) of weak-beam images can be estimated from the kinematical theory. For dislocations, an approximate value is[14]

$$\Delta x \cong \frac{0.28}{|s_g|}\left\{1 + \frac{K}{2(1-\nu)}\right\}$$

where ν is Poisson's ratio and $K = 0$ for a screw dislocation and 1 for an edge dislocation. Using $\nu = 1/3$ and $|s_g| = 2 \times 10^{-2}$ Å^{-1}, this formula gives the half-width of an edge dislocation as $\Delta x \cong 25$ Å which is a reasonable estimate for the computed images of Figs. 2 and 6.

§ 6.2. *Conditions determined by image peak position*

It has been shown in § 4 that the criterion $s_g + \boldsymbol{g} \cdot \mathrm{d}\boldsymbol{R}/\mathrm{d}z = 0$ at a turning point of $\boldsymbol{g} \cdot \mathrm{d}\boldsymbol{R}/\mathrm{d}z$ gives a good estimate for those parts of the lattice which produce an image peak. This relationship can be used to ensure that $|s_g|$ is sufficient large for the weak-beam peak to lie close to the individual cores. For example the image peak positions predicted by this criterion for an edge dislocation dissociated into two partials of Burgers vector $\boldsymbol{b}_1^{\mathrm{P}}$ and $\boldsymbol{b}_2^{\mathrm{P}}$ distance Δ_{D} apart, and taken with $\boldsymbol{g} \cdot \boldsymbol{b}_1^{\mathrm{P}} = \boldsymbol{g} \cdot \boldsymbol{b}_2^{\mathrm{P}}$, are

$$x = \{2 + C\Delta_{\mathrm{D}} \pm \sqrt{(4 + C^2\Delta_{\mathrm{D}}^2)}\}/2C$$

where

$$C = -s\Big/\left(\frac{(\boldsymbol{g} \cdot \boldsymbol{b}^{\mathrm{P}})}{2\pi}\left\{1 + \frac{1}{2(1-\nu)}\right\}\right).$$

The two solutions for x give the two image peak positions, and from these the systematic correction[1,6] which must be applied to the image peak separation to obtain the partial separation can be determined.

§ 6.3. *Diffraction conditions*

For a particular value of $|s_g|$ the diffracting conditions will vary for different materials and reflections. In general $s_g = (1 - n)\, g^2/2K$ where $K = 1/\lambda$ and the "reflection" ng is satisfied (where n need not be integral). For 100 keV electrons in copper, for example, an image taken with $g = 220$ has $|s_{220}| \cong 2 \times 10^{-2}$ Å^{-1} with either of the diffracting conditions shown in Figure 7a. But in the case of silicon the same value of $|s_{220}|$ requires the diffracting conditions shown in Figure 7b.

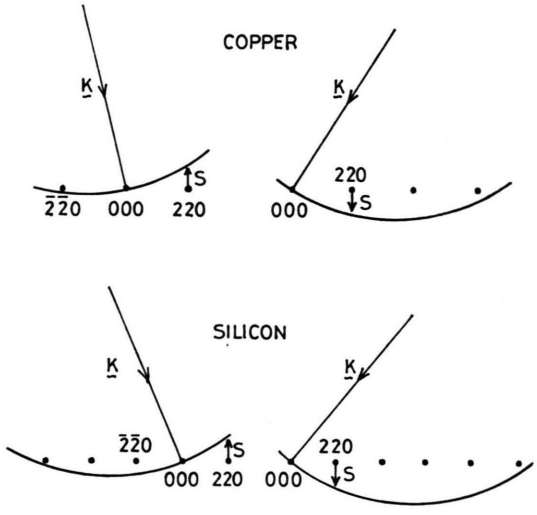

Fig. 7. The diffracting conditions in copper and silicon necessary to obtain $|s_{220}| \cong 2 \times 10^{-2}$ Å^{-1} for 100 keV electrons.

§ 7. Conclusions

The scattering processes which lead to weak-beam images have been discussed and the following conditions for obtaining weak-beam images have been derived.

1. The condition $|w| = |s\xi_g| \geqq 5$ leads to weak-beam images which give a qualitative picture of the defect geometry.

2. The prediction that an image peak occurs for those columns in which $s_g + \boldsymbol{g} \cdot (\mathrm{d}\boldsymbol{R}/\mathrm{d}z) = 0$ at a turning point of $\boldsymbol{g} \cdot (\mathrm{d}\boldsymbol{R}/\mathrm{d}z)$ can be used to determine the minimum value of $|s_g|$ required to ensure that the image peak lies sufficiently close to the dislocation core for a particular investigation.

3. The criterion for the image peak position given in (2) is an approximation, the accuracy of

which depends upon the nature of the strain field and $|s_g|$. For images of dislocations in which detail >25 Å is required, the criterion is satisfactory provided that $|s_g| \geqq 2 \times 10^{-2}$ Å^{-1}. The accuracy of the approximation improves with increasing $|s_g|$, but for more detailed analysis Eq. (8) can be used, or a comparison with computed images can be made.

4. In the two-beam case with $|s_g| \to \infty$, the weak-beam image is given by the kinematical theory. For large $|s_g|$, the image half-width and peak position can be determined to a first approximation from this theory.

5. Points 1 to 4 above apply to the case when the Ewald sphere does not pass close to any reciprocal lattice point. If this condition is not satisfied, the image may become more dependent on the defect depth and the foil thickness. There may be cases in which such effects are advantageous.

Weak-beam images taken under these conditions enable systematic investigation of dislocation geometries to be made at high resolution. It is clear that when the method is extended to studies of dislocation detail approaching $\simeq 15$ Å, more detailed analysis of Eqs. (6) and (8), and of their derivation, will be necessary.

Acknowledgements

I am grateful to Professor P. B. Hirsch, F.R.S., for much helpful advice during the course of this work, and for the provision of laboratory facilities, and to Drs. M. J. Whelan, I. L. F. Ray and A. P. Pogany for constructive criticism and comments upon details of the analysis. I am also grateful to the S.R.C. for financial support.

[1] D. J. H. Cockayne, I. L. F. Ray, and M. J. Whelan, Phil. Mag. **20**, 1265 [1969].
[2] D. J. H. Cockayne, J. R. Parsons, and C. W. Hoelke, Phil. Mag. **24**, 139 [1971].
[3] A. K. Head, Austr. J. Phys. **20**, 557 [1967].
[4] I. L. F. Ray and D. J. H. Cockayne, Proc. Roy. Soc. A **325**, 543 [1971].
[5] W. M. Stobbs and C. H. Sworn, Phil. Mag. **24**, 1365 [1971].
[6] D. J. H. Cockayne, M. L. Jenkins, and I. L. F. Ray, Phil. Mag. **24**, 1383 [1971].
[7] P. B. Hirsch, A. Howie, and M. J. Whelan, Phil. Trans. Roy. Soc. London A **252**, 499 [1960].
[8] A. Howie and C. H. Sworn, Phil. Mag. **22**, 861 [1970].
[9] C. J. Humphreys and P. B. Hirsch, Phil. Mag. **18**, 115 [1968].
[10] D. J. H. Cockayne, D. Phil. Thesis, Oxford University 1970.
[11] P. B. Hirsch, A. Howie, R. B. Nicholson, D. W. Pashley, and M. J. Whelan, Electron Microscopy of Thin Crystals, Butterworths, London 1965.
[12] A. Howie and Z. S. Basinski, Phil. Mag. **17**, 1039 [1968].
[13] M. Wilkens, Phys. Stat. Sol. **6**, 939 [1964].
[14] R. de Ridder and S. Amelinckx, Phys. Stat. Sol. **43**, 541 [1971].
[15] L. Pauling and E. B. Wilson, Introduction to Quantum Mechanics, Mc Graw Hill, New York 1935.
[16] R. W. Bicknell, Phys. Stat. Sol. **7**, K 1 [1971].